Journal of Power Sources 641 (2025) 236742

Contents lists available at ScienceDirect

Journal of Power Sources

journal homepage: www.elsevier.com/locate/jpowsour

Suppression of crystalline $Li_{15}Si_4$ in silicon-carbon composite anode with a Co-polymer binder for lithium ion batteries

Mohammad A. Islam [a,*], Joel Turallo [a], Junghoon Yang [b], Sang-Don Han [c]

[a] Department of Physics, State University of New York at Oswego, Oswego, NY, 13126, United States
[b] Carbon and Light Materials Application R&D Group, Korea Institute of Industrial Technology, Jeonju, 54853, Republic of Korea
[c] Department of Chemistry, Sejong University, Seoul, 05006, Republic of Korea

HIGHLIGHTS

- Co-polymerized polyimide P84 binder helps improve performance of silicon composite anode.
- P84 mediates compressive strain on the silicon-carbon anode from the copper current collector.
- A compressive stress of almost 1 GPa results in suppression of crystalline $Li_{15}Si_4$.
- Silicon composite anode with P84 binder suffers no runaway capacity drop.

GRAPHICAL ABSTRACT

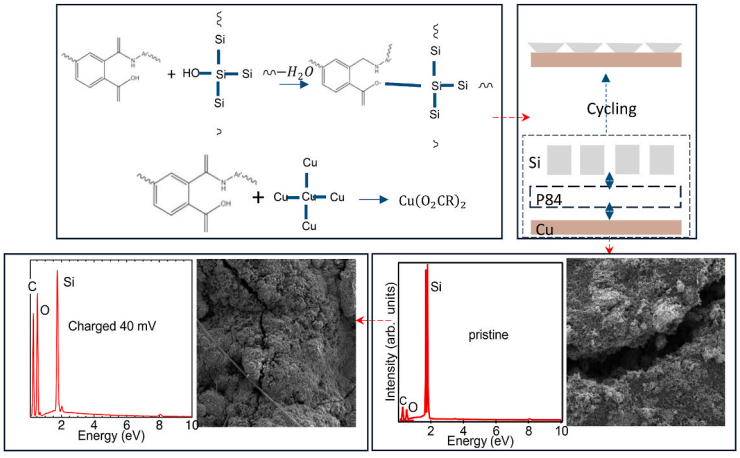

ARTICLE INFO

Keywords:
Lithium ion battery
Long cycle lives
Crystalline $Li_{15}Si_4$
Silicon-carbon composite anode
Co-polymerized polyimide binder

ABSTRACT

Suppression of crystalline $Li_{15}Si_4$ in silicon-carbon composite anode in lithium ion battery was achieved in electrochemical half-cells with an active material composed of 60 % nanosilicon, 20 % conductive carbon and 20 % P84 binder, and lithium metal counter/reference electrode. The half-cells were cycled between 1.5 V and 50 mV, the latter being the discharge voltage when crystalline $Li_{15}Si_4$ was found to form. Following this, the same cells were cycled between 1.5 V and 10 mV. A third set of cycling was carried out on the cells between 1.5 V and 5 mV. The gravimetric capacity was 1000 mAh/g after ninety cycles with the 50 mV discharge cutoff, 450 mAh/g after 200 additional cycles with 10 mV cutoff, and 300 mAh/g after 200 additional cycles with 5 mV cutoff. Unlike previous reports that showed precipitous drop of capacity accompanied by the formation of crystalline $Li_{15}Si_4$ the capacity drop in these cells was gradual. Cyclic voltammetry measurements carried out on the half-cells demonstrate the absence of sharp delithiation peak at 0.42 V that has been shown to indicate crystalline $Li_{15}Si_4$ formation. We provide supporting arguments of such absence of crystalline $Li_{15}Si_4$ via X-ray diffraction, Raman spectroscopy, field effect scanning electron microscopy/energy dispersive X-ray spectroscopy.

* Corresponding author.
E-mail address: mohammad.islam@oswego.edu (M.A. Islam).

https://doi.org/10.1016/j.jpowsour.2025.236742
Received 26 April 2024; Received in revised form 25 November 2024; Accepted 5 March 2025
Available online 21 March 2025

1. Introduction

The capacity of a lithium ion battery is approximately the parallel sum of that of the cathode and the anode [1]. The capacity of the current intercalation type cathode is in the range of 180 mAh/g and only incremental improvement in cathode capacity is being foreseen [2,3]. As such improving the anode capacity is one way to substantially improve the overall capacity. The current anode in lithium ion batteries is layered graphitic carbons, which, while adequate for small portable electronics and electric vehicles, suffer from several shortcomings, including low capacity (372 mAh/g) and incompatibility with some electrolytes accompanied by graphite exfoliation. Graphitic carbon, however, continues to be used in lithium ion batteries due to their high reversibility. A benchmark for anodes in lithium ion batteries has been established to be around 1000 mAh/g for high energy and power density applications, like advanced electric vehicles with long range. Silicon-based anodes can deliver such capacity [4–9].

The promise of silicon as high performance anode for next-generation lithium ion batteries is based on its low operating potential (~0.4 V *vs* Li/Li^+) close to that of graphite, a high theoretical capacity (>3500 mAh/g) through electrochemical alloying reactions with lithium, and its abundance in earth's crust [5]. Silicon, however, presents several challenges when used as anode in lithium ion batteries. Volumetric expansion up to ~300 % upon lithiation and concomitant shrinkage upon de-lithiation impart significant stresses and strains leading to pulverization of the anode and eventual detachment from the current collector. Silicon pulverization leads to other detrimental processes including continual formation of a thick and resistive solid-electrolyte interphase (SEI) on the newly created silicon fragments that involves consumption of unrecoverable Li ions [10,11]. Additional shortcoming of silicon is low diffusion kinetics of Li in silicon and its low intrinsic electronic conductivity.

The (de)lithiation of silicon is a complicated, multi-step process, and the formation of different lithiated phases depends on the depth of discharge and state of charge. These include, during lithiation, amorphous Li_xSi, amorphous $Li_{\sim 2.0}Si_4$, amorphous $Li_{15}Si_4$, and crystalline $Li_{15}Si_4$, and during delithiation, amorphous silicon. Formation of crystalline $Li_{15}Si_4$, that takes place below 50 mV, is especially important because it has been largely proved that this phase transition of silicon results in high internal stress that leads to particle fracture and cell capacity fade [7,10]. The formation of crystalline $Li_{15}Si_4$ and its dependence on silicon particle size and morphology, nanostructuring, substrate induced stress, and dopant addition has lately been a rich field of silicon anode research [7,10,12].

Experimental efforts to mitigate the detrimental effects of crystalline $Li_{15}Si_4$ were made through the application of nano-silicon [13–16]. It was found that anodes made of silicon nanoparticles of 150 nm diameter or less, nanowires of 300 nm diameter or less, and amorphous silicon films of less than 2.5 μ m thickness resulted in the suppression of crystalline $Li_{15}Si_4$. The variance in threshold sizes among various silicon nano-morphologies, however, raises practical question about the true nano-silicon size dependence of the suppression of crystalline $Li_{15}Si_4$. Perhaps as important from the point of view of practical application of nano-silicon anode is the ease and economy of the production of silicon nano-morphologies. Unlike the sol-gel process of III-V and II-VI semiconductor nanoparticles, successful growth of high quality silicon nanostructures requires ultra-high vacuum process and high temperature annealing in inert atmosphere, and as such economy of scaling of such process remains an open question. Alternative strategies in the form dopant addition, pretreating the electrode surface with SEI components and novel binders are being explored [17–21]. Despite these efforts, while silicon added in low quantities (~4–5 wt%) to graphite in commercial graphite-NMC cells is in the market, practical application of lithium ion battery anodes with high percentage of silicon remains a work in progress. Many reports showing improvement of silicon anode performance in lithium ion batteries show results of cycling under 100 cycles or so [9–11]. An older report of improved performance of silicon composite anode with in-situ polymerization of conducting hydrogel used ultra-low silicon coating of 0.2 mg/cm^2, significantly below industrial standard [22].

A more recent article by Choi et al., however, demonstrated good cycling behavior in silicon composite anode made with co-polymerized polyimide P84 binder. With very thin film of 0.6 mg/cm^2, they were able to achieve a capacity of 647 mAh/g after three hundred cycles [23,24]. The explanation for such improvement of electrochemical performance of silicon anode fabricated with aromatic binders were, to our judgement, inadequate with the focus mostly on the mechanical strength of the electrode slurry. For practical application of silicon anode in lithium ion batteries, cycling behaviors with many hundreds of cycles with capacity significantly above the graphite capacity of 372 mAh/g and subsequent explanation of electrochemical behavior with relevance to crystalline $Li_{15}Si_4$ is warranted. Such fundamental study was carried out by Sethuraman et al. [11]. Through combined theoretical modeling and experimental investigation, they determined the existence of stress-potential dependence in lithiated silicon. They estimated that a compressive stress of 1 GPa results in approximately 100 mV downshift of the silicon lithiation curve [12]. Since the formation of crystalline $Li_{15}Si_4$ takes place around 50 mV, if a silicon composite electrode were made with a built-in stress of 1 GPa, the formation of crystalline $Li_{15}Si_4$ can be largely suppressed. We argue in this paper that we have experimentally demonstrated the stress-potential relationship in electrochemical lithiation of silicon and consequent improvement of the performance of silicon-carbon composite anode in lithium ion electrochemical cells.

In this paper we demonstrate the suppression of crystalline $Li_{15}Si_4$ in silicon-carbon composite anode fabricated with the use of co-polymerized polyimide P84 binder, and a systematic and long-term curing of the binder. Electrochemical half-cells were fabricated using an active electrode composed of 60 % nanosilicon, 20 % conductive carbon and 20 % P84 binder (hereafter labeled silicon-carbon composite), and a punched lithium foil as the counter/reference electrode. When the half cells were cycled at C/10 rate between 1.5 V and 50 mV, the latter being the discharge voltage when crystalline $Li_{15}Si_4$ was found to be formed, we observed a capacity over 1000 mAh/g after ninety cycles. Unlike previous articles that showed precipitous drop of capacity accompanied by the formation of crystalline $Li_{15}Si_4$, the capacity drop in our half-cells was gradual. Following this, the same half-cells were further subjected to cycling between 1.5 V and 10 mV, which is significantly below the threshold of 50 mV. For this lower discharge voltage, we observed significant improvement of initial capacity and capacity retention of over 450 mAh/g after 200 additional cycles. We followed this with even lower discharge voltage cutoff of 5 mV and again we observed improvement of initial capacity and a capacity retention of just under 300 mAh/g after 200 additional cycles. Cyclic voltammetry measurements carried out on half-cells made of the silicon-carbon composite electrode showed absence of a sharp delithiation peak at 0.42 V that is well known to indicate the electrochemical formation of crystalline $Li_{15}Si_4$. Supporting arguments of such absence of crystalline $Li_{15}Si_4$ include analysis results of X-ray diffraction (XRD), Raman spectroscopy, and field effect scanning electron microscopy/energy dispersive X-ray spectroscopy (FESEM/EDS).

2. Experimental section

2.1. Materials and characterization

1-Methyl-2-pyrrolidinone (NMP, product # 328624) and silicon nanoparticles of average size 100 nm (product # 633097) were purchased from Sigma. Conductive carbon C45 was purchased from TIMCAL. Aromatic polyimide P84 binder was donated by Ensinger Sintimid GmbH. Lithium sheets were purchased from Fisher Scientific (product # AA1076722). The crystallinity of the silicon nanoparticles was

characterized using a Bruker Instruments X-ray diffractometer (Fig. 3). The morphology of the electrode slurry was investigated using a TESCAN MIRA field emission scanning electron microscope (FESEM). Lithiation of silicon anode was qualitatively studied through energy dispersive spectroscopy (EDS) assisted elemental mapping, utilizing the same TESCAN MIRA FESEM system.

2.2. Electrode and cell Fabrication

Slurries were made with 60 wt% silicon nanoparticles, 20 wt% C45 carbon black, and 20 wt% P84 binder. Since P84 does not dissolve in organic solutions easily, a concentrated solution of P84 was first prepared in NMP in the glovebox using a predetermined amount of P84 and NMP, and overnight mixing using a magnetic stirrer. Silicon nanoparticles, carbon black and P84 was mixed in a slurry mixer. Films of the slurry were fabricated by tape casting on carbon coated copper current collector. Since the performance of P84 as an electrode binder is known to depend on its curing scheme, a systematic post coating procedure was used to achieve the optimum mechanical and electrochemical properties of the silicon-carbon composite electrode. The tape cast electrode was placed in a vacuum oven and was dried for two days in room temperature with no vacuum applied. Following this, the electrode was dried under vacuum at a temperature of 150 °C for 24 h. Finally, the electrode was cured at a temperature of 350 °C under high pressure argon in a tube furnace for 4 h. Significant deviation from this scheme resulted in electrodes with low mechanical integrity (flaking off) and rapid capacity fade in the electrochemical cycling experiments. Typical mass loading of material on the electrode (15.5 mm diameter) was in the range 1.5–2.5 mg, and a typical electrode thickness was 10.2 μ m. The density of the active material on the finished electrode was thus in the range of 0.78 g/ml – 1.3 g/ml. This should be compared to the density of silicon which is 2.33 g/ml. Electrochemical coin-type cells were fabricated using these silicon-carbon composite slurry films as the working electrode, with an average material loading of 1.55 mg/cm^2, and punched lithium foil disks as the counter/reference electrode. One molar $LiPF_6$ (Sigma-Aldrich) in 50:50 vol% of ethylene carbonate (EC) and diethyl carbonate (DEC) was used as an electrolyte. A 3 wt% fluorinated ethylene carbonate (FEC) was used to improve the electrolyte performance. A Whatman GF/F glass fiber was used as the separator.

2.3. Electrochemical analysis and diagnostics

The cells were cycled galvanostatically at a rate of approximately C/10, which was 350 mA/g for silicon anode with a Li metal counter electrode, assuming an approximate full lithiation capacity of 3500 mAh/g[10]. All cells were subjected to initial three formation cycles, at a rate of C/10, between a voltage range of 1.5 V and 10 mV. After this the cells were cycled between an upper voltage of 1.5 V and variable lower voltages. To determine the formation of crystalline $Li_{15}Si_4$ in lithiated electrodes, upon arrival at a desired depth of discharge the cells were removed from the cycler. Each cell was then disassembled, and the electrodes retrieved. Following this, the electrodes were gently cleaned by using dimethyl carbonate (DMC, Sigma-Aldrich) for further characterizations. Cyclic voltammetry was carried out between 1.5 V and variable lower voltages (50 mV, 10 mV and 5 mV), at a scan rate of 0.2 mV/s.

2.4. Electrode crystal structure characterizations

X-ray diffraction (XRD) was carried out on the silicon-carbon composite electrode using a Brucker Instrument powder diffractometer. Raman spectra were excited using linearly polarized output of a solid state laser (785 nm) with 7 mW of power in a spot diameter of ≈1.0 μm at the sample and were dispersed and detected using a single-axis monochromator equipped with a charge-coupled detector array (Horiba XploRA, Edison NJ). All Raman spectra were collected unpolarized and in the backscattering geometry.

3. Results and discussion

3.1. Electrochemistry of silicon-carbon composite electrodes

3.1.1. Electrochemical behaviors based on lithium silicon alloying reactions

Electrochemical (de)lithiation of silicon is a multistep process and the specific phases of lithiated silicon and the subsequent delithiated phase depend on the depth of discharge and state of charge. The electrochemical lithiation of silicon results in, in progressive depth of discharge, amorphous silicon ($a-Si$), amorphous lithiated silicon alloy ($a-Li_{\sim 2.0}Si$), fully lithiated amorphous lithiated silicon ($a-Li_{\sim 3.5-3.75}Si$), and crystalline fully lithiated silicon alloy ($c-Li_{3.75}Si$).

Ogata et al. have reported the following major features of the differential capacity plots of silicon anodes in lithium ion batteries: high voltage coupled cathodic (c_2)//anodic (d_4) peaks at ~0.25 V–0.3 V// 0.55 V corresponding to the reactions $a-Si \rightarrow a-Li_{\sim 2.0}Si$// $a-Li_{\sim 2.0}Si \rightarrow a-Si$ and low voltage coupled cathodic (c_3)//anodic (d_2) peaks at ~0.1 V//0.3 V corresponding to the reactions $a-Li_{\sim 2.0}Si \rightarrow a-Li_{\sim 3.5-3.75}Si$// $a-Li_{\sim 3.5-3.75}Si \rightarrow a-Li_{\sim 2}Si$ [25]. The significant hysteresis in these reactions is a measure of energy dissipation, or in other words, the loss of cell efficiency. Traditionally the loss of cell efficiency has been ascribed to the overpotential required to drive a current at the electrode/electrolyte interfaces with its origin in sluggish kinetics and possible breaking of silicon bonds. A more recent explanation of the hysteresis was provided by Sethuraman et al. based on lithiation induced stress on silicon crystal and consequent change in its electrochemical potential [12].

Discharge below 50 mV results in cathodic peak c_4 corresponding to the reaction $a-Li_{3.75}Si \rightarrow c-Li_{3.75+\delta}Si$ and anodic peak d_3 corresponding to the asymmetric reaction $c-Li_{3.75+\delta}Si \rightarrow a-Li_{\langle 1.1}Si$. It has been shown that this last phase transformation of silicon that involves a crystalline highly lithiated material transforming to significantly lower lithiated amorphous silicide initiates inhomogeneous volume change and imparts intolerable strain on the silicon crystal that results in electrode degradation, detachment from the current collector and runaway capacity fade. The asymmetric anodic reaction d_3 manifests a sharp peak in the voltage range between 0.41 V and 0.43 V. We will specifically focus on the voltages where crystalline $Li_{15}Si_4$ is formed and is delithiated [5–10].

A first set of silicon-carbon composite anode based half-cells were subjected to cyclic voltammetry between 2.0 V and 50 mV. Selected CV plots are shown in Fig. 1 with appropriate labeling to indicate cycle numbers. Features cathodic c_2 and c_3, and anodic d_2, d_3, and d_4, are shown in the plot as vertical lines at positions described by Ogata et al. [25]. We note here that the voltage positions of the c_2, c_3, d_2, d_3, and d_4 peaks are approximate and they occur in a voltage range. Furthermore, the voltage positions of these peaks are known to shift as the electrochemical cycling progresses. Our focus in Fig. 1 is the d_3 peak and its relevance to crystalline $Li_{15}Si_4$.

The peak c_2 does not show up in the CV plots until the third cycle. Since initial lithiation corresponds to $c-Si \rightarrow a-Li_xSi$ the absence of this peak in the initial cycles is reasonable. We observe a gradually increasing negative peak below 50 mV starting from the very first cycles, indicating that $Li_{15}Si_4$ may have formed; whether this $Li_{15}Si_4$ is in amorphous or crystalline form is the critical issue of this paper and will be addressed shortly. Starting from the third cycle we observe clearly defined c_2//d_4 peaks in the range ~0.27 V//~0.52 V, and c_3//d_2 peaks at ~0.12 V//~0.33 V. It is noticeable that the c_2//d_4 peaks (especially the d_4 peak) are much more prominent compared to the c_3//d_2 peaks at the early cycles. Again, this is reasonable because at the beginning the cathodic//anodic reactions $a-Si \rightarrow a-Li_{\sim 2.0}Si$// $a-Li_{\sim 2.0}Si \rightarrow a-Si$ are prominent as more and more of the crystalline core of the silicon nanoparticles are lithiated with each cycles and more amorphous silicon is available for lithiation. Starting from the seventh cycle the d_4 peak

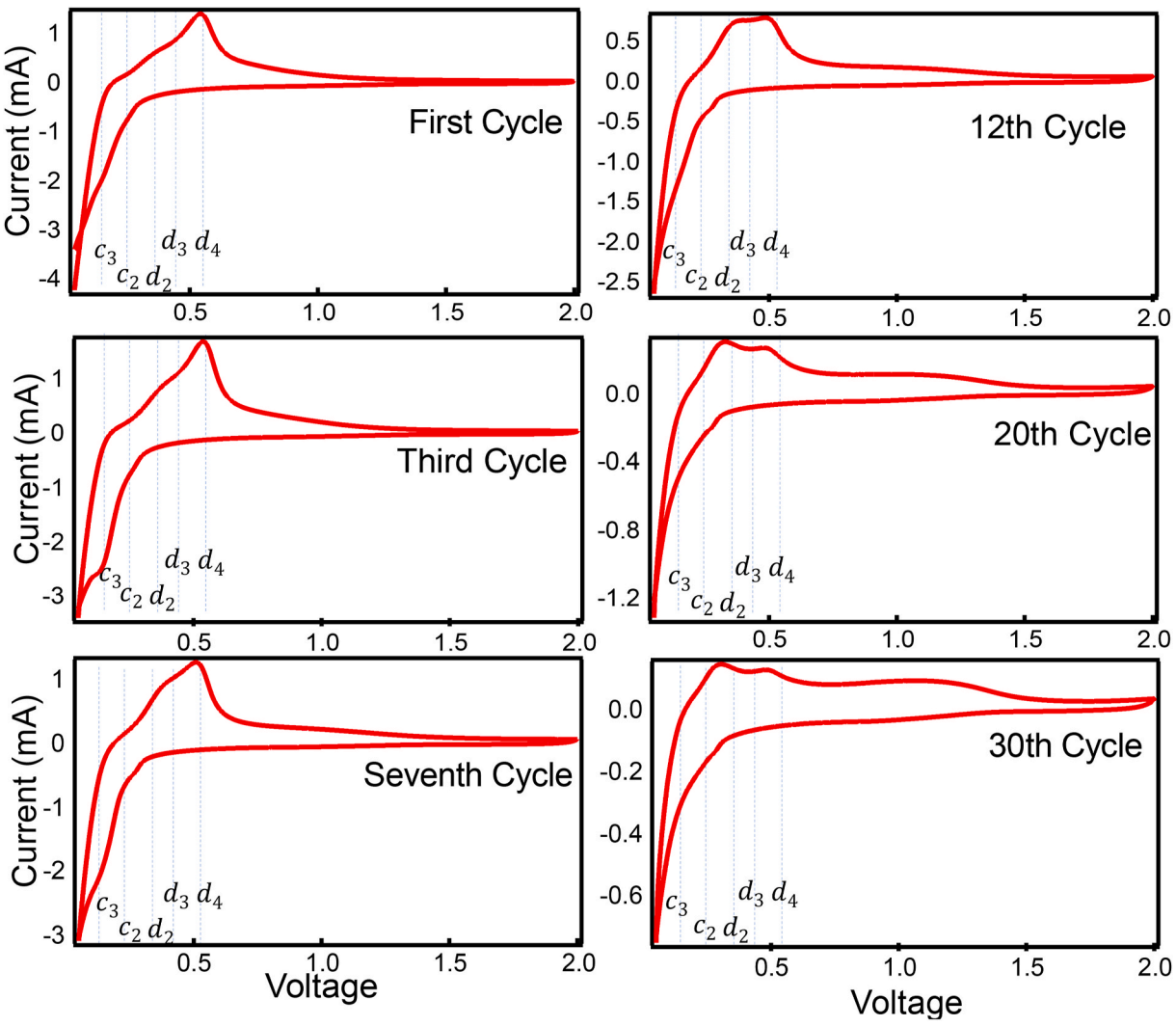

Fig. 1. Cyclic voltammetry (CV) of silicon-carbon anode based half-cells. CV was carried out on electrochemical half-cells with the silicon-carbon composite anode between 2.0 V and 50 mV with a scan rate of 0.2 mV/s. CV was also carried out on half-cells made of the same electrodes between 1.5 V and 10 mV (Fig. S1, Supplementary Information) and 1.5 V and 5 mV (Fig. S2, Supplementary Information) to detect the formation of crystalline $Li_{15}Si_4$. The vertical bars are the approximate literature values of the voltages where lithiation and delithiation of silicon takes place in the electrochemical cycling; d_3 is the anodic potential that indicates the delithiation of crystalline $Li_{15}Si_4$. (For interpretation of the references to colour in this figure legend, the reader is referred to the Web version of this article.)

starts to lose its comparative strength with the d_2 peak. At the 12th cycle the strengths of the d_4 peak and the d_2 peak are comparable, and by the 20th cycle the d_4 peak is significantly weaker than that of the d_2 peak. This all point towards progressive amount of crystalline silicon getting converted to amorphous silicon and at the same time more of the anode material being in highly lithiated form. Starting from the 30th cycle the CV plots reach a steady state. CV plots of cycles 45th through 50th almost perfectly overlap (not shown). Remarkable, however, is the absence of sharp and narrow peak d_3 in the anodic scan around 0.42 V, which indicates that *crystalline* $Li_{15}Si_4$ was not formed. The absence of sharp d_3 peak and the overlap of the CV plots beyond the 30th cycle point towards high performance of our silicon-carbon composite anode.

To determine possible formation of crystalline $Li_{15}Si_4$ at lower discharge voltages, we performed CV on two additional silicon carbon composite anode based half-cells, with gradually increasing depth of discharges of 10 mV and 5 mV. For this set of experiments the upper voltage was set to 1.5 V (partly to save time) since both the cathodic and anodic scans are flat beyond 1.5 V. The plots for these experiments are shown in the Supplementary Information Figs. S1 and S2; again, no anodic sharp peak (d_3) in the 0.41 V–0.43 V range is seen, indicating that crystalline $Li_{15}Si_4$ is not formed in the discharge half reactions. As has been shown previously, the formation of crystalline $Li_{15}Si_4$ is related to detachment of the active electrode material from the current collector that results in precipitous drop in capacity after few tens of cycles. As we show in the next section, our half cells demonstrate no such precipitous drop in cycles, and thus confirm the CV results.

3.1.2. *Long-term cycling performances for varying discharge cutoff voltages*

The capacity of silicon anode in lithium ion batteries depends on the depth of discharge. Initial electrochemical lithiation of crystalline silicon results in a two phase material with outer phase lithiated amorphous silicon ($a-Li_xSi$) surrounding crystalline silicon core. In the galvanostatic discharge curve this shows up as a slightly sloping voltage curve starting below 200 mV. Detailed study revealed that the capacity of this

plateau is in the range of 3250 mAh/g [5–10]. Continued lithiation below this plateau results in fully lithiated phase of silicon $Li_{15}Si_4$ with a maximum theoretical capacity of 3579 mAh/g, and deeper lithiation below 50 mV results in crystalline $Li_{15}Si_4$ [5–10]. Achievement of such high capacity, however, comes at a cost. The formation of crystalline $Li_{15}Si_4$ results in volume expansion of the original silicon crystal as much as 280 %, imparting significant stress on the electrode. On delithiation the electrode undergoes contraction. After several cycles, this volume change becomes unsustainable; the electrode gets pulverized in smaller pieces and eventually loses contact with the current collector. This result is runaway drop in the capacity reaching almost zero after few tens of cycles. Such precipitous drop in capacity is the ubiquitous nature of silicon anode in lithium ion batteries. Laboni et al. have shown that precipitous drop in capacity of silicon thin film anode in lithium ion half cells tracks very closely with the intensity of an anodic peak in the 0.42 V (peak d_3 in Fig. 1) range of the differential capacity plot. In other words, as crystalline $Li_{15}Si_4$ accumulates in the anode, runaway capacity fade takes hold [7].

Our electrochemical half-cells with silicon-carbon composite anode were first cycled galvanostatically at a rate of approximately C/10, in the voltage window of 1.5 V–50 mV. Selected charge/discharge plots are shown in Fig. 2a. The anode shows an initial gravimetric capacity of 2000 mAh/g that decreases gradually as the cycle progresses. The potential profiles of the discharge curves are characteristic of amorphous silicon with two sloping features and no evidence of crystalline $Li_{15}Si_4$ formation, and these are very similar to what Young et al. observed when they demonstrated suppression of crystalline $Li_{15}Si_4$ when LiF was added as a slurry additive in Si-Fe composite [8]. For better clarity we have plotted the first three cycles and cycles 60–64 in Figs. S3a and S3b in the Supplementary Information. These curves show no clearly defined flat plateau in the 0.42 V region in the charge cycles, indicating the absence of crystalline $Li_{15}Si_4$. Negligible amounts of intensities in the d_3 peak region in the CV plots in Fig. 1 and the absence of a flat plateau in the 0.42 V range in Figs. S3a and S3b corroborates each other and indicate that significant amount of crystalline $Li_{15}Si_4$ was not formed. After 90 cycles (Fig. 2a and b), the capacity is still over 1000 mAh/g, indicating negligible formation of crystalline $Li_{15}Si_4$.

The 50 mV discharge depth for the formation of crystalline $Li_{15}Si_4$ is an approximate value and has been found to change with the application of silicon nanostructures, slurry additive and substrate induced stress on the silicon electrode. Since we don't see a precipitous drop in capacity when we limited the discharge voltage to 50 mV, we continued cycling the same half-cell for another two hundred cycles, this time in the voltage window of 1.5 V and 10 mV. Selected charge/discharge plots for these set of runs are shown in Fig. S3c in the Supplementary Information, and the capacity determined from these plots are appended to Fig. 2b. As shown in Figs. S3c and 2b, the capacity with lower discharge voltage cutoff of 10 mV starts out from 2200 mAh/g and after 200 cycles the capacity is still 450 mAh/g. The reason for the capacity to go up to 2200 mAh/g from 1000 mAh/g, which was achieved at the end of the first set of cycling with 50 mV cutoff is clear; there is significant capacity originating from lithium silicon alloying reaction occurring between 50 mV and 10 mV. Similar to the cycling with 50 mV cutoff window, we see gradual drop of capacity, no 0.42 V plateau and no precipitous drop in capacity, indicating negligible formation of crystalline $Li_{15}Si_4$. A third set of cycling was carried out following the first two sets: this time with an even lower voltage cutoff of 5 mV (Figs. S3d and 2b). This resulted in a slightly higher initial capacity compared to the end of the cycles with 10 mV cutoff, no flat plateau in the 0.42 mV region and no precipitous drop in capacity, again indicating negligible formation of crystalline $Li_{15}Si_4$. It is remarkable that at end of additional two hundred cycles with 5 mV discharge cutoff voltage, the silicon-carbon composite anode demonstrated a capacity of almost 300 mAh/g (Fig. 2b).

Before moving onto the crystallographic analysis of the cycled electrodes we note that this paper is not about optimizing the capacity of silicon-carbon composite electrode. Our aim in this paper is the investigation of the suppression of crystalline $Li_{15}Si_4$ to improve lithium ion battery performance.

To verify the effects of electrode component ratio on the electrochemical performance, an additional two sets of electrodes were prepared with 40 wt% silicon nanoparticles, 40 wt% C45 carbon black, and 20 wt% P84 binder, and 20 wt% silicon nanoparticles, 60 wt% C45 carbon black, and 20 wt%

P84 binder, respectively, and evaluated as shown in Fig. S4. The capacity of half-cells made with these anodes showed high initial gravimetric capacity, but the capacity quickly faded and reached a capacity close to that of graphitic carbon at the end of the 80th cycle, possibly due to higher conductivity of carbon resulting in predominant

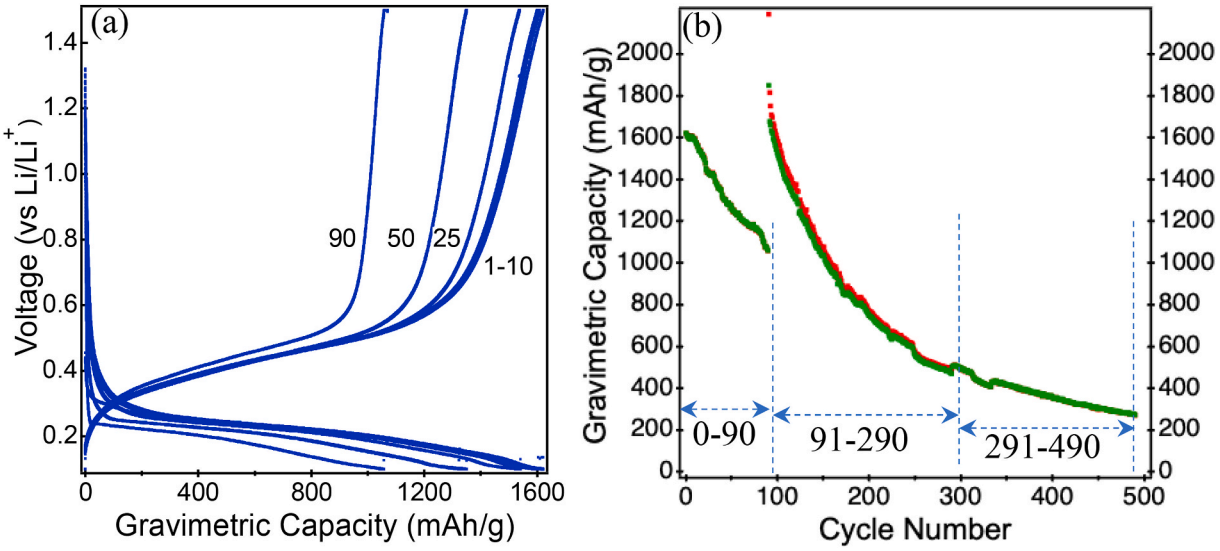

Fig. 2. Galvanostatic cycling. Electrochemical half-cells with silicon-carbon composite anode cycled galvanostatically at a rate of approximately C/10, in the voltage window 1.5 V to 50 mV (a) show an initial gravimetric capacity of 2000 mAh/g (b) that decreased to 1000 mAh/g at the end of 90 cycles. In Fig. 1a, charge/discharge plots of cycles 1–10, 25, 50 and 90 are shown. The same half cells were subjected to further cycling between 1.5 V and 10 mV (Fig. S3c, 200 more cycles) and between 1.5 V and 5 mV (Fig. S3d, 200 additional cycles). The capacities determined from these cycling are appended to Fig. 2b. (For interpretation of the references to colour in this figure legend, the reader is referred to the Web version of this article.)

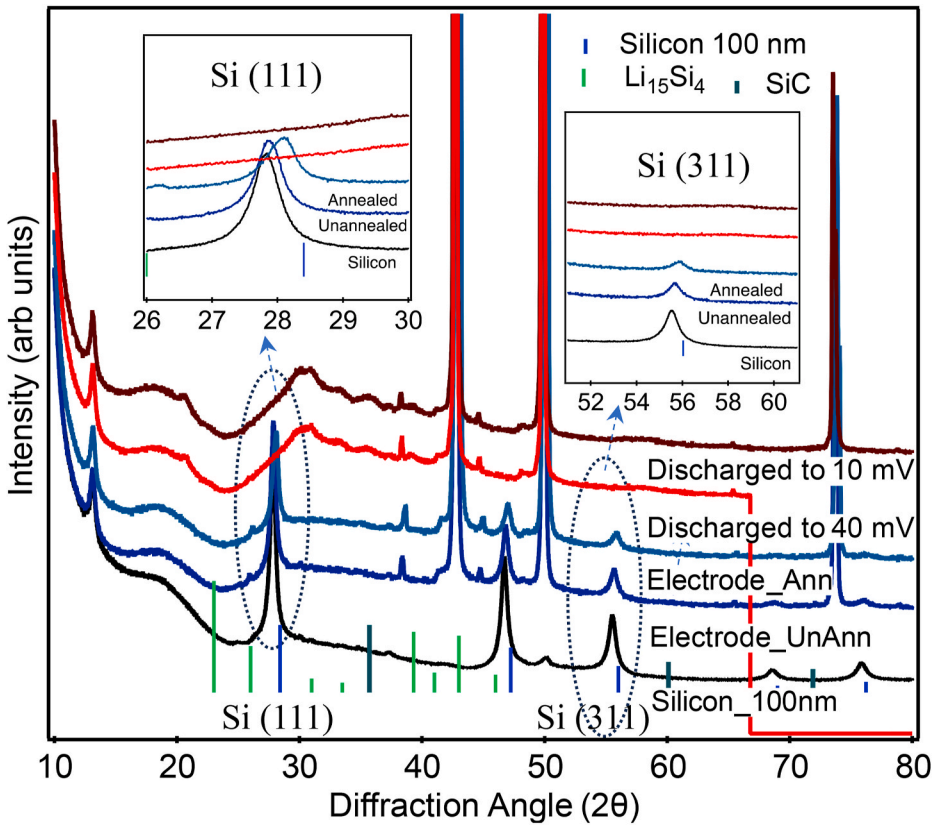

Fig. 3. XRD analysis of the silicon-carbon composite anode crystal structure. XRD patterns of the silicon nanopowders (average 100 nm diameter), and the pristine silicon-carbon composite anodes before and after annealing, and the cycled electrodes (discharged to 40 mV or 10 mV in each cycle). For reference, the prominent XRD features of silicon, $Li_{15}Si_4$ and SiC are also shown. XRD features of the Si (111) peak and Si (311) peak are shown with greater details as insets. (For interpretation of the references to colour in this figure legend, the reader is referred to the Web version of this article.)

carbon contribution to the overall capacity.

3.2. Effects of annealing step and electrochemical cycling on the formation of amorphous and crystalline $Li_{15}Si_4$ in the silicon-carbon composite electrodes

3.2.1. Strain and structure changes

XRD was carried out for the pristine silicon and fully discharged silicon-carbon composite electrodes (Fig. 3). The XRD peaks of the pristine silicon (average 100 nm diameter) are typical of what has been seen in other published results. Additional XRD analyses were carried out for the electrodes before and after annealing as shown in Fig. 3 with insets of XRD patterns for the Si (111) and (311) peaks. From the XRD measurements of Bragg reflection of the silicon powders, and the pristine electrodes before annealing and after annealing, we can extract information on the mechanical properties of the silicon-carbon composite anode.

X-ray diffraction vector q is related to the strain ε on material through $\varepsilon = -\Delta q/q$ [26]. As shown in the insets of Fig. 3, the XRD peaks of the silicon nanoparticles overlap well with those of the pristine electrode before annealing which is expected because the silicon crystal in the original nanoparticles and in

the unannealed film are essentially the same. The XRD features of the annealed film from both the (111) and (311) planes are, however, shifted to higher diffraction angles. Specifically, for the (111) plane we can determine an approximate shift in the reflection angle from $\theta = 13.92^\circ$ to $\theta = 14.015^\circ$. Using the Bragg diffraction condition, the strain *vs.* diffraction vector shift relationship, and the literature value of the Young's Modulus of silicon (111) wafer as 169 GPa we can determine a compressive stress of just under 1 GPa in the annealed film (detailed calculation in the Supplementary Information) [27]. As mentioned earlier Sethuraman et al. estimated that a compressive stress of 1 GPa results in approximately 100 mV downshift of the silicon lithiation curve. Considering the well-known results that formation of crystalline $Li_{15}Si_4$ occurs below 50 mV, such stress induced downshift of the voltage curve largely eliminates the formation of crystalline $Li_{15}Si_4$ with consequent improvement of anode performance. We believe the XRD results corroborates the cycling performance of the silicon-carbon composite anode (Fig. 2).

To detect the formation of amorphous silicon and/or crystalline $Li_{15}Si_4$ in the cycled electrodes XRD analyses were carried out for two sets of 60 cycled silicon-carbon composite anodes; the first set of electrodes were discharged to 40 mV in each cycle and the second set were discharged to 10 mV, in every cycle, respectively (Fig. 3). The XRD feature of amorphous silicon includes two broad peaks that encompass the 2θ regions of 20°–40° and 40°–60°. Obrovac et al. showed that when a silicon-based anode is lithiated below 50 mV, the XRD feature of silicon completely changed to multiple peak characteristics of the complicated crystal structure of crystalline $Li_{15}Si_4$. Based on Rietveld refinement of the XRD pattern from fully lithiated silicon fitted with the same structure as that of $Cu_{15}Si_4$, they determined the XRD line strengths of crystalline $Li_{15}Si_4$ [6]. We have included these in Fig. 3.

Fig. 3 clearly shows that the discharged electrodes contain mostly amorphous silicon as demonstrated by the broad feature between $2\theta = 20^\circ$ and 40°; the larger angle broad feature is not visible most probably because it is being overwhelmed by the substrate X-ray diffraction; in

this case the substrate being the copper current collector. Copper XRD have strong peaks at $2\theta = 44°$ and 51° [28]. More importantly the XRD patterns from the cycled electrodes show none of the crystalline $Li_{15}Si_4$ features, which corroborates the results of the cyclic voltammetry and the galvanostatic cycling results.

3.2.2. *Quantum confinement and chemistry*

Nano-scale unique properties of materials including quantum confinement, surface strain and chemistry are extremely important for battery performance, and these can be studied extensively utilizing Raman spectroscopy. To investigate the phase transformation of silicon-carbon composite anodes Raman analyses on the silicon powders, the pristine electrode before and after annealing, and the 60 cycled electrodes were performed. We start with a brief literature review of Raman spectra of crystalline silicon, amorphous silicon and crystalline $Li_{15}Si_4$.

Room temperature values of the zone-center phonon in crystalline silicon varies between 519 cm^{-1} and 522 cm^{-1}[29]. For nanoparticles the spectra show an asymmetry on the low energy side of the zone-center phonon that has been attributed to confinement effects and the effects of disorder caused by surface dangling bonds. Amorphous silicon Raman spectra consist of TA, LA, and TO strong bands centered around 150 cm^{-1}, 310 cm^{-1} and 480 cm^{-1} and a weak LO shoulder at 370 cm^{-1}[30]. Reports on the Raman spectra of crystalline $Li_{15}Si_4$ is, however, not widely available. $Li_{15}Si_4$ crystallizes in the $I\bar{4}3d$ (space group 220) structures with four formula units in the conventional unit cell. The system possesses Raman active modes A_1, E and T_2 with a total of six modes. Zeng et al. carried out Raman spectroscopy on crystalline $Li_{15}Si_4$ structure and found no Raman features in their study which they attributed to the metallic nature of $Li_{15}Si_4$ [29]. While it's true that $Li_{15}Si_4$ possess no bandgap at the Fermi level, absence of Raman features is not a must for materials with metallic band structures. Iron oxide Fe_3O_4 also has no bandgap at the Fermi

level but shows well developed zone center Raman modes [30].

Raman spectra of solid silicon (100) wafer (as a reference), the silicon nanopowders, the pristine silicon-carbon composite anodes before and after annealing, and the cycled anodes (discharged to 40 mV in every cycle) that was used in XRD studies are shown in Fig. 4. Raman spectra of solid silicon consist of a strong zone-center peak at 520.67 cm^{-1} and is very similar to what was seen in published articles [31, 32]. Raman spectra of silicon nanopowders with an average size of 100 nm and significant size dispersion show a zone center peak at 519.42 cm^{-1} with increased full width at half max (FWHM). The 1.25 cm^{-1} red shift of the zone center phonon compared to that of the bulk value can be attributed to tensile strained surface Si-Si bonds [31, 32].

Raman spectra of the pristine electrodes, before and after annealing, show significant difference from those of solid silicon wafer and nanopowders. The zone center mode is now at 513.19 cm^{-1} which is more than 6 cm^{-1} red shifted compared to silicon nanopowders. At first glance this seems to contradict the XRD results because the stress *vs*. Raman shift relationship [$\sigma\ (MPa) = -230\ \Delta\omega\ (cm^{-1})$] would suggest a tensile stress in the silicon-carbon composite anodes, even before they were annealed [26]. A closer look in this region (400 and 600 cm^{-1}), however, goes some way in mitigating this apparent contradiction (inset of Fig. 4). There is a negligible difference between the Raman shifts of the unannealed *vs*. annealed silicon-carbon composite anodes. We, therefore, argue that the red shift of the zone center phonon frequency of the silicon-carbon composite anodes from that of the silicon nanopowders is originated from the intricacies of the vibrational modes of nanosilicon, not related to electrochemical reactions or substrate induced strain.

Red shift of Raman modes in confined systems is a well-known

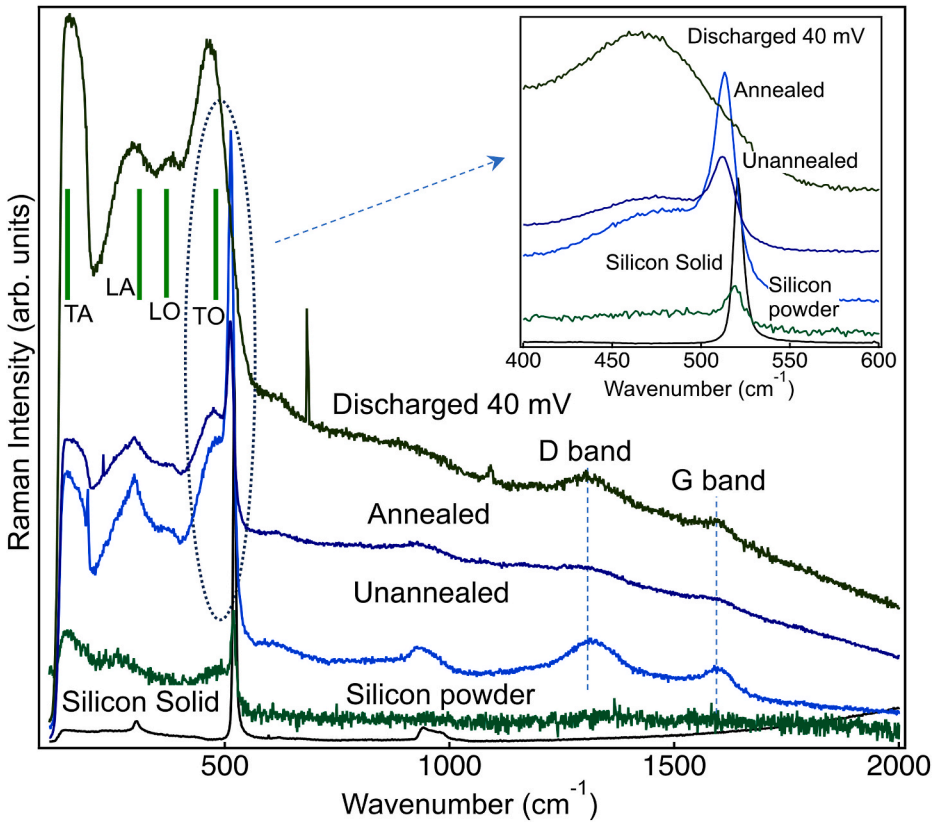

Fig. 4. Raman analysis of the silicon-carbon composite anode crystal structure. Raman spectra of solid silicon (100) wafer (as reference), silicon nanopowders, the pristine silicon-carbon composite anodes before and after annealing, and the cycled anodes (discharged to 40 mV in every cycle). Raman spectra between 400 and 600 cm^{-1} is shown with greater details as inset. The TA, LA, LO, and TO modes of amorphous silicon are shown as vertical lines. (For interpretation of the references to colour in this figure legend, the reader is referred to the Web version of this article.)

phenomenon. Campbell et al. has calculated confinement induced redshift of the optical phonon in silicon hemispherical nanoparticles and for 2 nm size particles, and they estimated the red-shift value to be 5 cm^{-1}[33]. Experimental values of Raman peak red shift in 10 nm size Co_3O_4 nanoparticles was found to vary between 6 cm^{-1} and 30 cm^{-1}, depending on the particular mode symmetry [33]. While our silicon nanoparticles have average size of 100 nm, significantly larger than those used in the previous studies [34,33], some confinement induced red shift is expected. In addition, it is well known that Raman spectroscopy is a surface sensitive process and as such it is likely that we are sampling a small fraction of the silicon-carbon composite electrode from the top while the strain effects owing to the substrate is nor being probed. We argue that the interaction of poly(amic acid) through its -COOH group with the silanol group of the silicon nanopowder creates a strong confinement effect which is responsible for such large red shift in the Raman feature of the silicon-carbon composite electrode. We elaborate more on the bonding schemes of poly(amic acid) with silicon nanoparticles in the next section. The issues of confinement induced shift, however, has less bearing on the thrust of this article, which is the suppression of crystalline $Li_{15}Si_4$ in silicon-carbon composite anode. We now turn to the Raman spectra of the cycled anodes.

Raman spectra of the cycled electrode show all the three strong broad bands of amorphous silicon at positions close to what have been seen in previous studies [32]. In the spectra of the cycled electrode as well as the un-annealed and annealed electrodes we observe two broad features of carbon D and G bands at Raman shifts positions that are well known. No sharp peaks indicative of crystalline nature of $Li_{15}Si_4$, however, are seen in the Raman spectra of the cycled electrode. The Raman results thus corroborate the results of the cyclic voltammetry and the galvanostatic charge and discharge results (Figs. 1 and 2).

We note that all Raman spectra were collected at the same laser power and as such we can rule out laser heating induced shift of the Raman lines. Photographs of the samples before and after the collection of Raman spectra were taken to observe signs of laser induced burning of the samples and there were none.

3.3. Fundamental and mechanistic understanding of enhanced electrochemical performance

3.3.1. Role of copolymerized polyimide P84 binder

It is important to understand how the application of the P84 binder could result in strong compressive strain on the silicon-carbon composite slurry from the substrate with consequent suppression of crystalline $Li_{15}Si_4$ in electrochemical cycling. The P84 binder is based on 3,3′ 4,4′ - benzophenone tetracarboxylic dianhydride with 80 wt% toluene di-isocyanate and 20 wt% methylene diphenyl di-isocyanate co-polyimide precursor (BTDA-TDI/MDI, Fig. 5a). These aromatic binders are prepared by curing (imdizing) poly(amic acids) by a condensation reaction in the temperature range of 250 °C–400 °C. The unique feature of aromatic polyimides is their mechanical flexibility, good surface coverage and most importantly, adhesion to both current collectors and silicon alloys that is mediated by the carboxyl group of the poly(amic acids). Specifically, poly (amic acids) reacts with copper to make copper carboxylate ($Cu(O_2CR)_2$), which results in strong adhesion to copper current collector. The adhesion of poly (amic acids) to silicon alloy is mediated by the carboxyl group of the former and the silanol group (S-OH) on the surface of silicon nanoparticles to form strong ester groups, as shown in Fig. 5b. Evidently these dual properties of the P84 binder results in a (comprehensively) strained silicon-carbon composite film, as shown schematically in Fig. 5c, lower panel. As we discuss in the next section, lithiation induced volume increase in the comprehensively strained silicon-carbon film is accommodated by lateral expansion of the film (Fig. 5c, upper panel).

In addition to these chemical properties, aromatic binders possess distinct electrochemical properties as well. It was suggested by Wilkes et al. that aromatic binder like polyimides and phenolic resins, when used as a component of the silicon based anode in lithium ion batteries, undergo full reduction resulting in hydrogen containing carbon with the latter creating an in situ carbon coating around the silicon particles [35]. As a result, electrochemical properties of silicon alloy anodes improve significantly when aromatic binders are used. For polyimides Wilkes

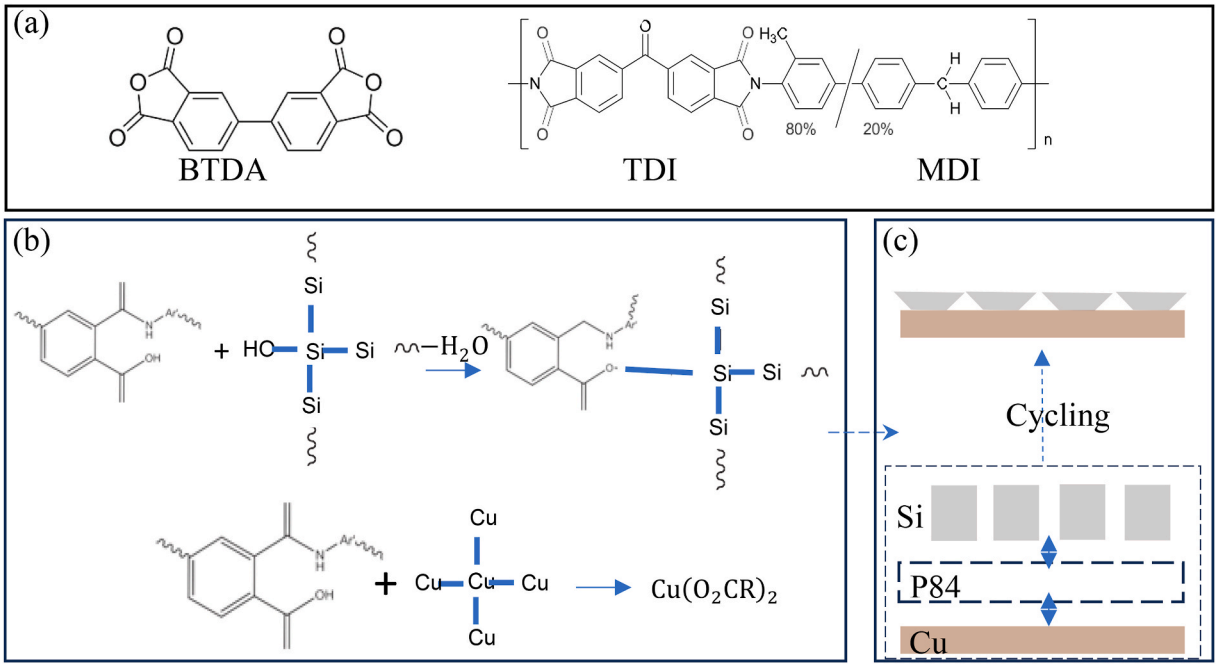

Fig. 5. The chemical structure of the P84 co-polymerized polyimide binder is shown in Fig. 5(a). Mechanism of poly(amic acid) adherence to silicon anode and the copper collector (b). Application of P84 binder results in a (compressively) strained silicon-carbon slurry on cooper current collector (c). Prior to cycling the silicon-carbon composite electrode has the morphology of a dried film that cracks due to solvent evaporation (c, lower panel). As cycling progresses lithiation induced volume increase in the comprehensively strained silicon-carbon film is accommodated by lateral expansion of the film (c, upper panel). (For interpretation of the references to colour in this figure legend, the reader is referred to the Web version of this article.)

et al. determined a first cycle lithiation capacity of 2000

mAh/g and reversible capacity of less than 400 mAh/g. The improvement of electrochemical activity of silicon with polymeric aromatic binder, however, is found to depend significantly on the choice of aromatic binder, curing temperature, degree of aromaticity and the polymer precursor.

Since we used the P84 binder in our experiment, first we determined how much of the capacity shown in Fig. 2 could have been contributed by the binder alone. Assuming the specific capacity of the P84 binder we used in our experiment to be the same as that of the polyimide binder Wilkes et al. used in their study, the maximum capacity contributed by P84 at the 60th cycle in Fig. 2 would be about 6.4 % of the total. For the calculation, please see the Supplementary Information. We can thus rule out the possibility of a significant amount of capacity shown in Fig. 2 to be contributed by the binder alone. On the other hand, suppression of crystalline $Li_{15}Si_4$ was found to be highly dependent on cell polarization that can result from

increased rate of cycling and high impedance when a thick SEI layer is formed on the silicon electrode. We have carried out cycling at moderate rate of C/10 and as such we assume that cell polarization was not a significant factor in the suppression of crystalline $Li_{15}Si_4$. We thus believe the suppression of crystalline $Li_{15}Si_4$ and the consequent improvement of the electrochemical performance of our silicon-carbon composite electrode is a result of strong compressive strain on the silicon composite slurry from the current collector, mediated by the P84 binder.

3.3.2. *Morphology and mechanical property*

FESEM analysis was conducted on the pristine and cycled (discharged to 40 mV in every cycle) electrodes. Fig. 6a of the pristine electrodes show an electrode morphology that is typical of that of a dried composite slurry that develops cracks once the solvent dries. Higher magnification image of Fig. 6b shows that the cracks are 10 μm wide and has a uniform width as these propagates through the film. Fig. 6e and f are typical images of the cycled electrode. The contrast between Fig. 6a, b and 6e, 6f is clear. In Fig. 6e the cracks have shrunk significantly, and we see from Fig. 6f that the plates of the electrodes are now overlapping each other. We believe the overlapping of the

plates as seen in Fig. 6f is a result of the silicon carbon composite slurry being anchored to the current collector at the bottom of the film and being relatively free at the top. As demonstrated through the XRD

results (Fig. 3) the silicon-carbon slurry in under a strong compressive strain from the substrate that could result from the bonding of the slurry to the copper current collector mediated by the P84 binder. We also argued through Raman studies (Fig. 4) that the surface of the electrode film is comparatively free. As silicon gets progressively lithiated and form Li_xSi the silicon anode starts to swell, and since the electrode in anchored at the bottom of the current collector, the swelling results is the anode material expanding laterally across the electrode surface. And this results in filling up of the initial cracks and overlapping of the electrode plates. This is also shown schematically in Fig. 5c. We claim the FESEM figures provide further proof of the electrochemical cycling, the XRD and the Raman results.

Fig. 6c is a typical higher magnification image of the pristine electrode and Fig. 6g is that of the cycled electrode. It is clear from Fig. 6c that vast majority of the particles are in the size regime of 100 nm, which is the typical size of the silicon particles we used for our experiment. As seen in Fig. 6g most of the particles in the cycled electrode are at least twice the size of those in Fig. 6c. Comparison of Fig. 6c with Fig. 6g confirms the well-known lithiation induced expansion of silicon when used as an anode in lithium ion batteries.

Energy dispersive spectroscopy (EDS) was carried out on the pristine anode and the cycled electrode. The contrast between the pristine electrode and the cycled electrode is clear in the EDS analysis of the elements. As seen in Fig. 6d, in the pristine electrode the strength of the silicon line is much stronger than that of the oxygen line and the

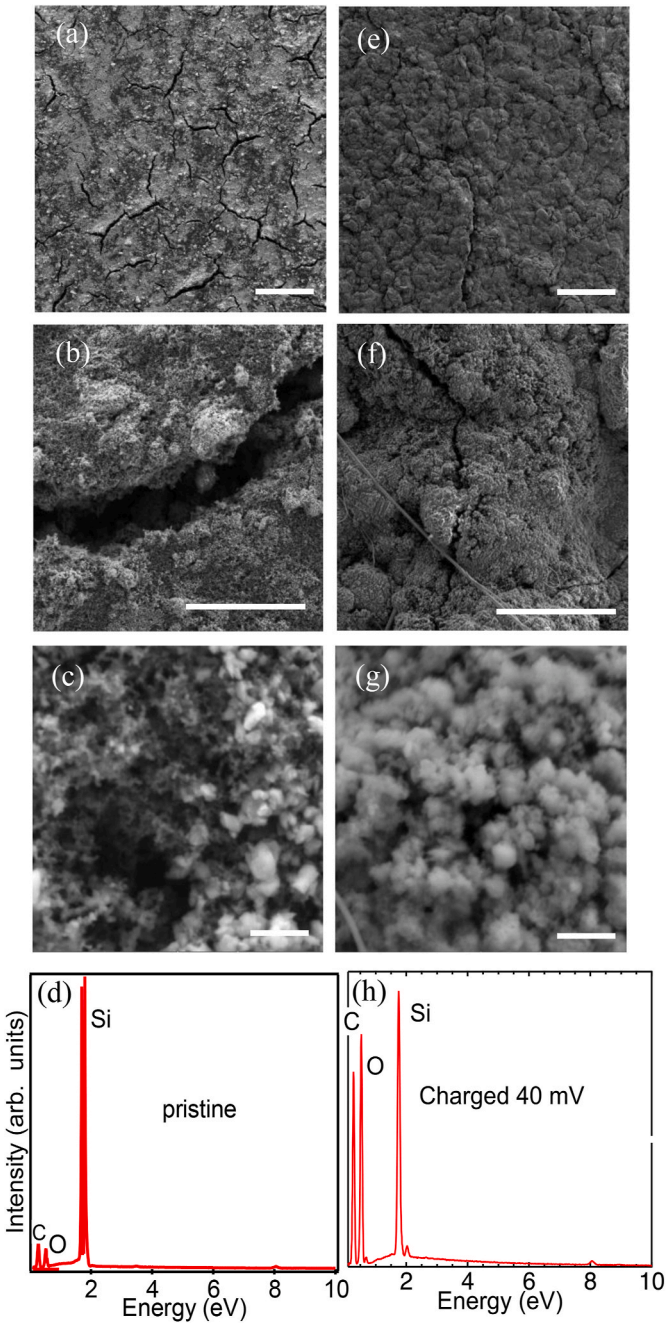

Fig. 6. FESEM of silicon-carbon composite electrode at different stages of cycling reveals the electrochemical phase transformation of silicon. Fig. 6a, b and 6c are images of the pristine film and Fig. 6e, f and 6g are images of the lithiated film. Comparison of 6b with 6f shows that cracks shrink significantly upon lithiation. Comparison of 6c with 6g shows that the silicon particles expand significantly upon lithiation. Comparison of the EDS elemental mapping Fig. 6d of the pristine film with Fig. 6h of the lithiated anode shows the prevalence of oxygen on the surface of the silicon particles in the lithiated anode. The magnification bars in Fig. 6a and e are 100 μ m, in Fig. 6b and f are 20 μ m, Fig. 6c and g are 400 n m. (For interpretation of the references to colour in this figure legend, the reader is referred to the Web version of this article.)

strengths of the oxygen line is comparable to that of the carbon line. Since in the slurry mixer we used 60 % silicon, 20 % carbon and 20 % P84, we believe the EDS elemental analysis is reasonable. In the cycled electrode the strength of the oxygen line is again comparable to that of the carbon line, as seen in Fig. 6h. The strength of the oxygen line is now, however, comparable to that of the silicon line. Peak fitting of the EDS

elemental mapping of Fig. 6d and h shows that the ratio of oxygen to silicon line strengths is approximately ten times in the cycled electrode compared to that in the pristine electrode. The improved strength of the oxygen line in the cycled electrode points to the efficiency of the P84 binder in forming chemical bonding with the silicon particles mediated by oxygen rich carboxyl group.

4. Conclusion

High performance silicon-carbon composite anodes were formulated using copolymerized polyimide P84 binder and a systematic and long-term curing scheme. Half-cells composed of the silicon-carbon composite anode and lithium foil counter/reference electrode demonstrated high gravimetric capacity compared to the current state-of-the art graphitic carbon anode. Unlike previous attempts at electrochemical cycling of silicon based anodes with high percentage of silicon, the capacity did not suffer runaway fading. We associate this improved performance of the silicon-carbon composite anode with the suppression of crystalline $Li_{15}Si_4$ that is known to be detrimental to the electrochemical cycling of silicon anode in lithium ion battery. Through a combination of XRD, Raman spectroscopy and FESEM/EDS we demonstrated that the suppression of crystalline $Li_{15}Si_4$ has its origin in the compressive stress resulting from bonding of the electrode slurry to the copper current collector mediated by the P84 binder.

CRediT authorship contribution statement

Mohammad A. Islam: Writing – review & editing, Writing – original draft, Visualization, Validation, Supervision, Software, Resources, Project administration, Methodology, Investigation, Funding acquisition, Formal analysis, Data curation, Conceptualization. **Joel Turallo:** Investigation, Formal analysis, Data curation. **Junghoon Yang:** Writing – review & editing, Investigation, Formal analysis, Data curation. **Sang-Don Han:** Writing – review & editing, Investigation, Funding acquisition, Formal analysis, Data curation, Conceptualization.

Declaration of competing interest

The authors declare that they have no known competing financial interests or personal relationships that could have appeared to influence the work reported in this paper.

Acknowledgements

This work was partially supported by the National Science Foundation Platform for the Accelerated Realization, Analysis, and Discovery of Interface Materials (PARADIM) under Cooperative Agreement No. DMR-2039380. This work was supported by the faculty research fund of Sejong University in 2023.

Appendix A. Supplementary data

Supplementary data to this article can be found online at https://doi.org/10.1016/j.jpowsour.2025.236742.

Data availability

Data will be made available on request.

References

[1] U. Kasavajjula, C. Wang, A. Appleby, Nano- and bulk-silicon-based insertion anodes for lithium-ion secondary cells, J. Power Sources 163 (2007) 1003–1039, https://doi.org/10.1016/j.jpowsour.2006.09.084.
[2] D. Rogstad, Mari-Ann Einarsrud, A. Svensson, Evaluation of selected ionic liquids as electrolytes for silicon anodes in Li-ion batteries, J. Electrochem. Soc. 168 (2021) 110506, https://doi.org/10.1149/1945-7111/ac330f.
[3] Y. Ding, Z.P. Cano, A. Yu, J. Lu, Z. Chen, Automotive Li-ion batteries: current status and future perspectives, Electrochem. Energy Rev. 2 (2019) 1–28, https://doi.org/10.1007/s41918-018-0022-z.
[4] C. Chan, C, H. Peng, G. Liu, K. McIlwrath, X.F. Zhang, R.A. Huggins, Y. Cui, High-performance lithium battery anodes using silicon nanowires, Nat. Nanotechnol. 3 (2008) 31–35, https://doi.org/10.1038/nnano.2007.411.
[5] M.N. Obrovac, Si-alloy negative electrodes for Li-ion batteries, Curr. Opin. Electrochem. 9 (2018) 8–17, https://doi.org/10.1016/j.coelec.2018.02.002.
[6] M.N. Obrovac, L. Christensen, Structural changes in silicon anodes during lithium insertion/extraction, Electrochem. Solid State Lett. 7 (2004) A93–A96, https://doi.org/10.1149/1.1652421.
[7] D.S.M. Iaboni, M.N. Obrovac, $Li_{15}Si_4$ formation in silicon thin film negative electrodes, J. Electrochem. Soc. 163 (2016) A255–A261, https://doi.org/10.1149/2.0551602jes.
[8] R.S. Young, B. Scott, C. Wei, M.N. Obrovac, LiF as an alloy component or slurry additive in Si-alloy anodes, J. Electrochem. Soc. 167 (2020) 160524, https://doi.org/10.1149/1945-7111/abcf56.
[9] Z. Du, R.A. Dunlap, M.N. Obrovac, Structural and electrochemical investigation of Fe_xSi_{1x} thin films in Li cells, J. Electrochem. Soc. 163 (2016) A2011, https://doi.org/10.1149/2.0961609jes.
[10] M.N. Obrovac, L.J. Krause, Reversible cycling of crystalline silicon powder, J. Electrochem. Soc. 154 (2007) A103–A108, https://doi.org/10.1149/1.2402112.
[11] J.W. Choi, D. Aurbach, Promise and reality of post-lithium-ion batteries with high energy densities, Nat. Rev. Mater. 1 (2016) 16013, https://doi.org/10.1038/natrevmats.2016.13.
[12] V.A. Sethuraman, V. Srinivasan, A.F. Bower, P.R. Gudurua, In situ measurements of stress-potential coupling in lithiated silicon, J. Electrochem. Soc. 157 (2010) A1253, https://doi.org/10.1149/1.3489378. A126.
[13] M. Piwko, T. Kuntze, S. Winkler, S. Straach, P. Härtel, H. Althues, S. Kaskel, Hierarchical columnar silicon anode structures for high energy density lithium sulfur batteries, J. Power Sources 351 (2017) 183, https://doi.org/10.1016/j.jpowsour.2017.03.080.
[14] G. Mu, Z. Ding, D. Mu, B. Wu, J. Bi, L. Zhang, H. Yang, H. Wu, F. Wu, Hierarchical void structured Si/PANi/C hybrid anode material for high-performance lithium-ion batteries, Electrochim. Acta 300 (2019) 341–348, https://doi.org/10.1016/j.electacta.2019.01.126.
[15] N. Harpak, G. Davidi, D. Schneier, S. Menkin, E. Mados, D. Golodnitsky, E. Peled, F. Patolsky, Large-scale self-catalyzed spongelike silicon nano-network-based 3D anodes for high-capacity lithium-ion batteries, Nano Lett. 19 (2019) 1944–1954, https://doi.org/10.1021/acs.nanolett.8b05127.
[16] K. Ababtain, G. Babu, X. Lin, M. Rodrigues, H. Gullapalli, P. Ajayan, M. Grinstaff, L. Arava, Ionic liquid–organic carbonate electrolyte blends to stabilize silicon electrodes for extending lithium ion battery operability to 100 °C, ACS Appl. Mater. Interfaces 8 (2016) 15242, https://doi.org/10.1021/acsami.6b02620.
[17] H.F. Andersen, C.E.L. Foss, J. Voje, R. Tronstad, T. Mokkelbost, P.E. Vullum, A. Ulvestad, M. Kirkengen, J.P. Mæhlen, Silicon-Carbon composite anodes from industrial battery grade silicon, Sci. Rep. 9 (2019) 14814, https://doi.org/10.1038/s41598-019-51324-4.
[18] M.H. Parekh, V.P. Parikh, P.J. Kim, S. Misra, Z. Qi, H. Wang, Vilas G. Pol, Encapsulation and networking of silicon nanoparticles using amorphous carbon and graphite for high performance Li-ion batteries, Carbon 148 (2019) 36, https://doi.org/10.1016/j.carbon.2019.03.037.
[19] D. Kim, M. Park, S.-M. Kim, H.C. Shim, S. Hyun, S.M. Han, Conversion reaction of nanoporous ZnO for stable electrochemical cycling of binderless Si microparticle composite anode, ACS Nano 12 (2018) 10903–10913, https://doi.org/10.1021/acsnano.8b03951.
[20] B. Wang, J. Ryu, S. Choi, X. Zhang, D. Pribat, X. Li, L. Zhi, S. Park, R.S. Ruoff, Ultrafast-charging silicon-based coral-like network anodes for lithium-ion batteries with high energy and power densities, ACS Nano 13 (2019) 2307–2315, https://doi.org/10.1021/acsnano.8b09034.
[21] M. Piwko, S. Thieme, C. Weller, H. Althues, S. Kaskel, Enabling electrolyte compositions for columnar silicon anodes in high energy secondary batteries, J. Power Sources 362 (2017) 349, https://doi.org/10.1016/j.jpowsour.2017.07.046.
[22] H. Wu, G. Yu, G.L. Pan, et al., Stable Li-ion battery anodes by *in-situ* polymerization of conducting hydrogel to conformally coat silicon nanoparticles, Nat. Commun. 4 (2013) 1943, https://doi.org/10.1038/ncomms2941.
[23] J. Oh, D. Jin K. Kim, D. Song, M.-H. Ryou, Improving the cycling performance of lithium-ion battery Si/graphite anodes using a soluble polyimide binder, ACS Omega 2 (2017) 8438–8444, https://doi.org/10.1021/acsomega.7b01365.
[24] J. Choi, K. Kim, J. Jeong, K. Cho, M.-H. Ryou, Y. Lee, Highly adhesive and soluble copolyimide binder: improving the long-term cycle life of silicon anodes in lithium-ion batteries, ACS Appl. Mater. Interfaces 7 (2015) 14851–14858, https://doi.org/10.1021/acsami.5b03364.
[25] K. Ogata, S. Jeon, Ds Ko, et al., Evolving affinity between Coulombic reversibility and hysteretic phase transformations in nano-structured silicon-based lithium-ion batteries, Nat. Commun. 9 (2018) 479, https://doi.org/10.1038/s41467-018-02824-w.
[26] S. Tardif, E. Pavlenko, L. Quazuguel, M. Boniface, M. Maréchal, J.-S. Micha, L. Gonon, V. Mareau, G. Gebel, P. Bayle-Guillemaud, F. Rieutord, S. Lyonnard, *Operando* Raman spectroscopy and synchrotron X-ray diffraction of lithiation/delithiation in silicon nanoparticle anodes, ACS Nano 11 (2017) 11306–11316, https://doi.org/10.1021/acsnano.7b05796.
[27] W. Bentley, Calculated elastic constants for stress problems associated with semiconductor devices, J App, Phys. Met. 44 (1973) 534, https://doi.org/10.1063/1.1661935.

[28] R. Phul, C. Kaur, U. Farooq, T. Ahmada, Ascorbic acid assisted synthesis, characterization and catalytic application of copper nanoparticles, Material Sci & Eng Int J. 2 (2018) 90–94, https://doi.org/10.15406/mseij.2018.02.00040.

[29] Z. Zeng, Q. Zeng, N. Liu, A. Oganov, Q. Zeng, Y. Cui, W. Mao, A novel phase of $Li_{15}Si_4$ synthesized under pressure, Adv. Energy Mater. 5 (2015) 1500214, https://doi.org/10.1002/aenm.

[30] M.A. Islam, J. Bouldin, J. Yang, S.-D. Han, Electrochemical sodiation mechanism in magnetite nanoparticle-based anodes: understanding of nanoionics-based sodium ion storage behavior of Fe_3O_4, ACS Materials and Interfaces 14 (2022) 50773–50782, https://doi.org/10.1021/acsami.2c13016.

[31] D. Bimberg, in: O. Madelung, et al. (Eds.), Numerical data and functional relationships in science and technology, Landolt-Bornstein, New Series, Group III, 17i, Springer, Berlin, 1982, p. 72.

[32] A. Sirenko, J. Fox, I. Akimov, X. Xi, S. Ruvimov, S, Z. Liliental-Weber, In situ Raman scattering studies of the amorphous and crystalline Si nanoparticles, Solid State Commun. 113 (2000) 553–558, https://doi.org/10.1016/S0038-1098(99)00539-6.

[33] M.A. Islam, M. Zuba, V. DeBiase, N. Novisky, C. Hawley, High capacity lithium ion batteries composed of cobalt oxide nanoparticle anodes and Raman spectroscopic analysis of nanoparticle strain dynamics in batteries, Nanotechnology 29 (2018) 075403, https://doi.org/10.1088/1361-6528/aaa231.

[34] I. Campbell, P. Fauchet, The effects of microcrystal size and shape on the one phonon Raman spectra of crystalline semiconductors, Solid State Commun. 58 (1986) 739, https://doi.org/10.1016/0038-1098(86)90513-2.

[35] B. Wilkes, Z. Brown, L. Krause, M. Triemert, M. Obrovac, The electrochemical behavior of polyimide binders in Li and Na cells, J. Electrochem. Soc. 163 (2016) A364–A372. http://hdl.handle.net/10222/81780.